

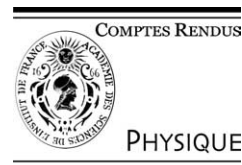


ELSEVIER

Available online at [www.sciencedirect.com](http://www.sciencedirect.com)

SCIENCE @ DIRECT®

C. R. Physique 5 (2004) 325–335



PHYSIQUE

Highly polarized nuclear spin systems and dipolar interactions in NMR/Systèmes de spins nucléaires fortement polarisés et interactions dipolaires en RMN

## Relaxation measurements by magnetic resonance force microscopy

Olivier Klein\*, Vladimir V. Naletov

Service de physique de l'état condensé, CEA Orme des Merisiers, 91191 Gif-Sur-Yvette, France

Available online 17 April 2004

### Abstract

The spatial resolution of magnetic resonance imaging can be greatly enhanced by replacing the coil antenna (or cavity) with a scanning force microscope. We describe how this mechanical detection can be applied to the measurement of both the transverse and longitudinal relaxation inside a micron-size volume. The measurement procedure and analysis is detailed for the case of paramagnetic and ferromagnetic spin systems. **To cite this article:** O. Klein, V.V. Naletov, *C. R. Physique 5 (2004)*.

© 2004 Académie des sciences. Published by Elsevier SAS. All rights reserved.

### Résumé

**Mesure de la relaxation par microscopie à résonance magnétique détectée mécaniquement.** La résolution spatiale d'un imageur à résonance magnétique peut être fortement améliorée en remplaçant l'antenne à bobine (ou cavité) par un microscope à force atomique. Nous décrivons comment cette détection mécanique peut être appliquée à l'étude de la relaxation transversale et longitudinale dans des échantillons microscopiques. Le protocole de mesure et d'analyse est décrit pour des spins paramagnétiques et ferromagnétiques. **Pour citer cet article :** O. Klein, V.V. Naletov, *C. R. Physique 5 (2004)*.

© 2004 Académie des sciences. Published by Elsevier SAS. All rights reserved.

**Keywords:** Magnetic Resonance Force Microscopy; Spin relaxation; Magnetic Resonance Imaging

**Mots-clés :** Microscopie à Résonance Magnétique détectée Mécaniquement ; Relaxation magnétique ; Imagerie par Résonance Magnétique

### 1. Introduction

The Nobel prize of medicine was awarded in 2003 to the two physicists Paul Lauterbur [1] and Peter Mansfield [2] for their discoveries in 1973 concerning magnetic resonance imaging (MRI). Foreseeing the benefits of placing the sample in an inhomogeneous magnetic field was indeed very counter intuitive. One beautiful experiment that suffered from being discovered prior to their work, is the first mechanical detection of nuclear paramagnetic resonance (NMR) by Evans in 1955 [3]. At that time, Evans [3] was looking for new ways of measuring the static component of the nuclear susceptibility. Inspired by the Faraday balance, he proposed to place the sample in a magnetic field gradient to generate a force on it. The sensitivity of his apparatus was found to be comparable to a coil detection. In its concluding remarks, he noted that his new technique "however, (was) unlikely to have any practical importance, since an inhomogeneous field is necessary and therefore the (spectral) resolution is excessively low". Further development on the mechanical method, were obtained by Alzetta et al. in 1967 [4,5]. They reported the detection of electron paramagnetic resonance (EPR) in diphenylpicrylhydrazil (DPPH). Here the sample was placed in a homogeneous field and the torque was measured.

These ideas were revisited more recently by Sidles [6] in the light of the progress made both on MRI and on atomic force microscopy (AFM). Having a detector sensitive to the magnetic field gradient [7] should allow high spatial resolution in an extremely inhomogeneous field. He proposed to use a micro-fabricated cantilever to mechanically detect the resonance with a

\* Corresponding author.

E-mail addresses: [olivier.klein@cea.fr](mailto:olivier.klein@cea.fr) (O. Klein), [vnaletov@cea.fr](mailto:vnaletov@cea.fr) (V.V. Naletov).

nanometer scale spatial resolution. The new technique is referred to as magnetic resonance force microscopy (MRFM) [8]. The first magnetic resonance force signal was detected by Rugar et al. in 1992 while exciting EPR in a 30ng crystal of diphenylpicrylhydrazil [9]. Two years later, Rugar et al. reported the mechanical detection of  $^1\text{H}$  (protons) NMR in 12ng of ammonium nitrate [10]. These two experiments demonstrated that AFM cantilevers can be a substantial improvement over the coil detection.

After a short introduction to MRFM with a comparison between force and coil detection, we describe how this technique can be applied to the measurements of the dissipative term that enters in the equation of motion for the magnetization vector. It is shown that measurements of both the transverse and longitudinal spin dynamics can be obtained for paramagnetic and ferromagnetic spins systems.

## 2. Principle of the mechanical detection of magnetic resonance

More precisely, MRFMs are inspired by the magnetic force microscope, a variant of the AFM. A micron-size permanent magnet is affixed at the free end of a clamped cantilever and placed in the stray field of the sample. The induction at the tip location,  $\mathbf{B} = \mathbf{B}_{\text{ext}} + \mathbf{B}_M$ , is the superposition of an homogeneous external field,  $\mathbf{B}_{\text{ext}}$  (applied along the  $z$ -axis), and the inhomogeneous dipolar field,  $\mathbf{B}_M$ , produced by the sample magnetization  $\mathcal{M}$ . The resulting point load on the tip induces an elastic deformation of the cantilever. For a uniform magnetization  $\mathcal{M}$  throughout the volume of the permanent magnet (e.g., if the strength of the external field is well above its saturation field), the force and torque acting on the tip takes respectively the form:

$$\mathbf{F} = \oint_{S_{\text{tip}}} \mathbf{B}(\mathcal{M} \cdot \mathbf{n}) dS, \quad (1a)$$

$$\mathbf{N} = \int_{V_{\text{tip}}} (\mathcal{M} \times \mathbf{B}) dV, \quad (1b)$$

with  $V_{\text{tip}}$  the volume of the tip and  $S_{\text{tip}}$  its surface of unit normal  $\mathbf{n}$ . Changes in the deformation are monitored when the magnetic resonance is electromagnetically excited in the sample. The Larmor resonance  $\omega_0$  usually occurs at a frequency that is several orders of magnitude higher than the fundamental flexural mode of the cantilever. The motional mass of the tip at  $\omega_0$  then is very large and the mechanical probe is insensitive to the precession of the transverse component of the sample magnetization,  $M_t$ . The mechanical deformation is only produced by the correlative decrease of the longitudinal component (i.e., along the precession axis)  $M_s - M_z$ ,  $M_s$  being the static magnetization at thermal equilibrium.

In the standard configuration, the axis of freedom of the cantilever is oriented parallel to the static field ( $z$  direction). If we define the  $x$ -axis as the direction along the length of the cantilever, then  $F_z$  and  $N_y$  are the two components of the force and torque producing a deformation in the  $z$  direction. The quantity measured is the pitch angle,  $\alpha$ , at the free end of the cantilever. For a simple beam cantilever of length  $l$ ,  $\alpha$  can be expressed through the formula:

$$\alpha = \frac{l^2}{2EI} F_z + \frac{l}{3EI} N_y, \quad (2)$$

with  $E$  and  $I$  respectively the Young modulus and the quadratic moment of the cantilever.

In our experiments, the probe-sample interaction uses some further simplifications. The experiments reported below are performed on a configuration that has axial symmetry. On the symmetry axis, the  $x$ -component of the dipolar field ( $\mathbf{B}_{M_z} \cdot \hat{\mathbf{x}}$ ) vanishes and it does not contribute to the torque ( $N_y = 0$ ). Assuming further that the permanent magnet is a cylinder aligned lengthwise with  $z$  (see Fig. 1), then Eq. (1a) integrates into

$$F_z = A_{\text{tip}} \mathcal{M} \Delta B_z, \quad (3)$$

with  $A_{\text{tip}}$  the area of the generative section and  $\Delta B_z$  the field difference across the length of the magnetic bar. If this length is small compare to the sample probe separation, then the changes in the deformation are proportional to the field gradient  $g$  produced by the  $M_z(r)$  profile of the sample.

Our discussion begins with a review of the arguments that sustain the use of a cantilever instead of a coil to detect magnetic resonance in microscopic samples.

## 3. Sensitivity of the force detection

The relevant quantity here is the signal to noise ratio ( $SNR$ ). Both a coil and a force detection use the magnetic coupling of the spin system to a linear oscillator. Sidles and Rugar derived a common expression for the sensitivity [7]

$$SNR \propto M V_{\text{slice}} \frac{\sqrt{\omega Q/k_m}}{\sqrt{4k_B T \Delta f}}. \quad (4)$$

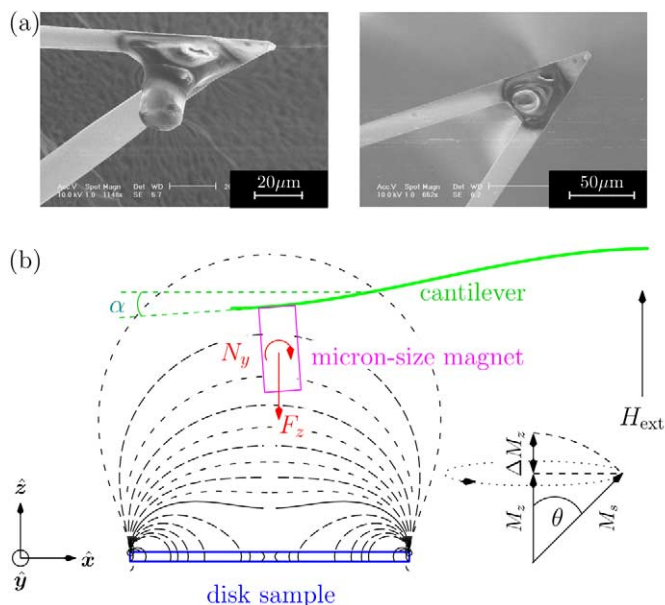


Fig. 1. (a) Images of the probe magnet glued onto the cantilever. (b) Model of our setup showing the iso-field lines of the sample stray field ( $z$  component) for a uniformly magnetized disk. The change of the pitch angle  $\alpha$  measures the diminution of the sample longitudinal magnetization  $M_s - M_z$ . The deformation of the cantilever on the figure is greatly exaggerated: typical value of  $\alpha$  are around  $10^{-6}$  rad.

The pre-factor is proportional to the number of spins, with  $M$  the magnitude of the sample magnetization ( $M_t$  for a coil,  $M_s - M_z$  for a cantilever) and  $V_{\text{slice}}$  is the resonating slice (inversely proportional to the field gradient for paramagnetic spins). The denominator represents the thermal noise ( $T$  the temperature and  $k_B$  the Boltzman constant) inside the detection bandwidth,  $\Delta f$ . The probe itself is characterized by a resonance frequency,  $\omega$ , a quality factor,  $Q$ , and a magnetic stiffness  $k_m$ . Low magnetic stiffness for the oscillator means that the probe uses very little storage energy to change the magnetic field at the sample location. The stiffness of a coil is given by  $k_m \approx V_{\text{coil}}/2\pi$  [7]. A cantilever changes the local field by displacing the probe magnet to another location and  $k_m = k/g^2$  [7] with the  $k$  the mechanical spring constant. This expression illustrates the interest of using a cantilever for MRI. An increase of the magnetic field gradient  $g$ , improves the spatial resolution but does not deteriorate the  $SNR$ . The loss in  $V_{\text{slice}}$  associated with the increase of  $g$  is compensated by the decrease of  $k_m$ .

Using Eq. (4), we review briefly how to modify the oscillator geometry to increase the  $SNR$ . All things being equal it is always advantageous to have  $\omega$  as large as possible. Coils (or cavities) can easily detect signals at r.f. or microwave frequencies and they are used as detector of the dynamic susceptibility (i.e., around the Larmor frequency). In contrast commercial cantilevers are at present limited to the low end of the r.f. spectrum. There has been, so far, only reports about the static susceptibility using a force detection. Going to large  $\omega$  for a cantilever requires mainly to reduce its mass. Independent studies about the mechanical properties [11] of carbon nanotubes quote frequencies as large as 2 GHz [12], although detecting such movements is still difficult [12]. It is useful to note that, in some cases, the measurement of the static susceptibility is more important. We will give examples of such cases when we discuss ferromagnetic resonance.

Eq. (4) clearly states that  $k_m$  should be minimized. For a coil, that implies reducing its volume. There is actually an optimum for the  $SNR$  when the coil fits the given sample size. It corresponds to the highest filling factor. However, from a fabrication point of view, it is difficult to create windings below the micron scale [13]. For a 60  $\mu\text{m}$  inner diameter planar microcoil [14]  $k_m \approx 10^{-10}$  cm<sup>3</sup>. In comparison, the spring constant  $k$  of a cantilever depends as the cube of the ratio thickness over length of the beam. Some of the thinnest cantilevers micro-fabricated [15] (0.17  $\mu\text{m}$  thick) have a spring constant which is of the order of  $k \approx 10^{-4}$  N/m in zero field. For tip sample separation of the order of 1  $\mu\text{m}$ , the gradient of field produced is of the order of  $g \approx 10^5$  T/m, which leads to  $k_m \approx 10^{-15}$  cm<sup>3</sup>: a substantial improvement over coil detection.

We note that the  $SNR$  ratio also depends on the quality factor,  $Q$ , of the oscillator. External parameters (e.g., the temperature or the pressure) can influence greatly the value of  $Q$ . The  $Q$  of a coil decreases when its size is reduced because both the inductance  $L$  and the electrical conductance  $\sigma$  of the windings decrease. For example, the planar microcoils mentioned above have a  $Q \approx 1$  [16]. The use of a superconducting material improves somewhat the result, but then the damping becomes dominated by the penetration of magnetic flux vortices inside the coil [17]. The  $Q$  of a cantilever also decreases with size. It depends on the thickness but it is reasonably independent of the length or width of the cantilever [15]. Taking again the case

of the  $0.17\ \mu\text{m}$  thick single crystal silicon cantilever, the  $Q$  is about  $10^4$  at room temperature. This suggests that the physical process responsible for the damping in cantilevers are among the smallest for these kinds of length scale [18].

The last important point concerns the detector noise. Eq. (4) assumes that the  $SNR$  is set by the thermal fluctuations on the probe oscillator and not by the amplification electronics after. This is indeed true for a mechanical detection. Both a laser beam deflection scheme, or a fiber optic interferometer add an amplifier noise that is several orders of magnitude lower than the intrinsic thermal noise of a soft cantilever. But these types of amplifier are difficult to build at higher frequencies. They usually involve sophisticated equipment based on a maser or parametric amplifier [19].

Overall a dimensional analysis [18] shows that cantilevers are better detectors compare to coils when it comes to volume size below the micron scale. The smallest cantilevers available [15] have already the sensitivity to detect single spins, albeit in stringent conditions: vacuum, large field and sub-Kelvin temperatures. But new difficulties arise when the coupling between the spins systems and the probe increases to the level of a single spin detection. Going to a very large gradient with very soft cantilever means approaching a fluctuating (e.g., Brownian motion [20]) permanent magnet close to the sample. It limits the probe sample separation to a few hundred nanometers. Although single spin *sensitivity* might be achievable in the case of diluted paramagnetic spin systems [21,22], important challenges remain ahead before reaching true atomic resolution. In short, the spatial resolution limit of MRFM is still unclear [23]. Progress on the matter will probably depend on the understanding of the relaxation process associated with the approach of a permanent magnet near the sample surface.

In the following, we describe how to measure these parameters for paramagnetic and ferromagnetic spin systems.

#### 4. Studies of paramagnetic spin systems

##### 4.1. NMR force detection setup

The setup that used in this section corresponds to a sample on cantilever approach [24] (see Fig. 2). The experiment is performed at room temperature inside a vacuum cell ( $10^{-2}$  torr). The instrument fits between the poles of an iron core electromagnet which produces a static magnetic field  $B_{\text{ext}} \approx 0.9\ \text{T}$  along  $z$ . To the uniform field we add a second inhomogeneous field,  $B_{\text{cyl}}$ , with axial symmetry produced by a magnetized iron cylinder 8 mm in length and 1.9 mm in diameter. The bar is

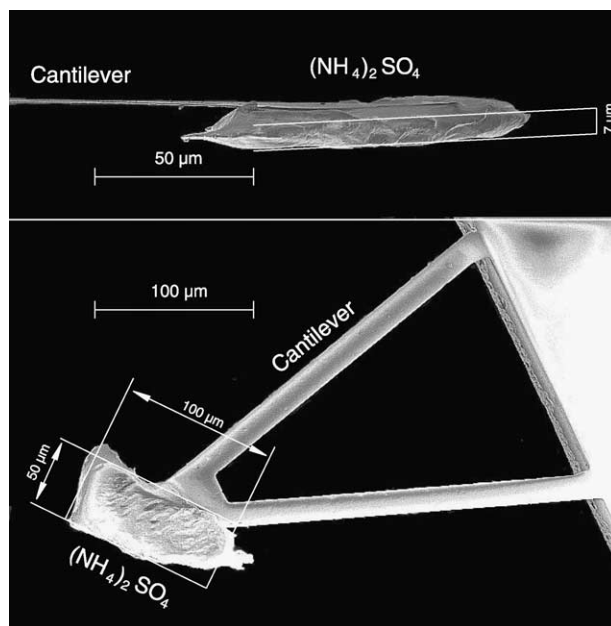


Fig. 2. Image of a commercial  $\text{Si}_3\text{N}_4$  (amorphous) cantilever: a  $7\ \mu\text{m}$  thick single-crystal of  $(\text{NH}_4)_2\text{SO}_4$  sample is glued on the cantilever's end with epoxy. The loaded cantilever has a resonance frequency of  $1.4\ \text{kHz}$ , a spring constant of  $0.008\ \text{N/m}$  and a quality factor of  $4000$  in vacuum. From the images in Fig. 2, the sample dimensions are  $100 \times 50 \times 7\ \mu\text{m}^3$  with the smallest length (actually the thickness) oriented along the axial field, which corresponds to  $N \approx 10^{15}$  protons.

centered 0.70 mm below the sample. The polarization field along the axis is  $B_0 = B_{\text{ext}} + B_{\text{cyl}} \approx 1.3\text{T}$  and the instantaneous magnetic force acting on the sample is given by a variant of Eq. (1a):

$$F(t) = \int_{V_s} M_z(\mathbf{r}, t) \frac{\partial B_{\text{cyl}}}{\partial z} dV, \quad (5)$$

with  $M_z$  the  $z$  component of the bulk magnetization and  $V_s$  the volume of the sample. For small sample size, we make the approximation that the field gradient  $g = \partial B_{\text{cyl}}/\partial z \approx 470\text{ T/m}$  is constant over  $V_s$ . We define a new length variable  $\zeta = B_0(\mathbf{r})/g$  constant on surfaces (paraboloids) of constant polarization field so that nuclear spins that are located at the same  $\zeta$  value always share similar time variation of their bulk magnetization.

Our test compound is a  $(\text{NH}_4)_2\text{SO}_4$  crystal cleaved to a platelet aspect ratio and glued with epoxy on the end of a soft cantilever as can be seen in Fig. 2.

#### 4.2. The c.w. measurement sequence

$M_z$  is modulated at  $\omega_c$ , the frequency of the fundamental flexure mode of the cantilever. The modulation is generated by a continuous-wave (c.w.) sequence that consists of periodic adiabatic fast passages [25]. The radio-frequency (r.f.) source of a Voltage Controlled Oscillator (VCO) is amplified up to 7 W and fed into an impedance matched resonating circuit ( $Q_{\text{rf}} \simeq 100$ ) tuned to a fixed frequency, 54.7 MHz. A small coil (3 turns, 0.8 mm in diameter) is in series with the tank circuit. The sample is 0.5 mm away from this antenna. The nuclear spin are irradiated for a few seconds by a linearly polarized r.f. field  $B_x = 2B_1 \cos\{\int_0^t \omega(t') dt'\}$  with  $\omega(t) = \Omega \sin(\omega_c t) + \omega_0$ , a sine-wave modulation of the r.f. frequency around the proton Larmor frequency  $\omega_0 = \gamma g \zeta_0$ , where  $\gamma/2\pi = 4.258\text{ kHz/G}$  is the nuclear gyromagnetic ratio (see Fig. 3). The surface of constant  $\zeta = \zeta_0$  is called the resonant sheet. We consider that the sinusoidal frequency modulation is started at time  $t = 0$ . In a transformation to a rotating coordinate system  $(i, j, k)$  with an instantaneous angular velocity  $\omega(t)\mathbf{k}$ , the effective magnetic field is:

$$\mathbf{B}_e(\zeta, t) = B_1 \mathbf{i} + \left\{ g\zeta - \frac{\omega(t)}{\gamma} \right\} \mathbf{k}. \quad (6)$$

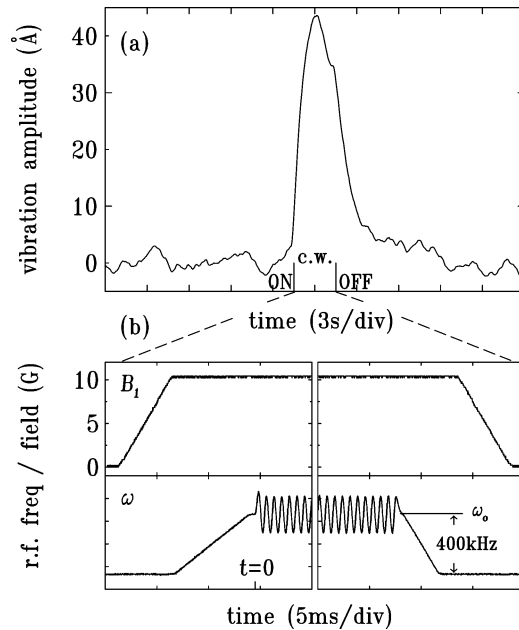


Fig. 3. (a) Vibration amplitude of the cantilever measured by the lock-in for a  $(\text{NH}_4)_2\text{SO}_4$  crystal containing  $10^{15}$  protons at 300 K in  $B_{\text{ext}} = 0.9425\text{ T}$ . The trace corresponds to a single shot experiment with no averaging. (b) Details of the start and end of the c.w. sequence. The crystal is irradiated for 3 s by a r.f. field of  $B_1 = 10\text{ G}$  (upper panel). The bottom panel shows the frequency waveform applied to the VCO around  $\omega_0/2\pi = 54.7\text{ MHz}$ . The amplitude of the frequency modulation is  $\Omega/2\pi = 150\text{ kHz}$ .

We define  $\theta$  as the polar angle made by the effective field with the external field. Provided that we are in the adiabatic regime, the spin system remains at all times in a state of internal equilibrium and  $\mathbf{M}$  is parallel to  $\mathbf{B}_e$  as required by Curie's law. The longitudinal magnetization is  $M_z(\zeta, t) = |\mathbf{M}| \cos \theta$ , where

$$\cos \theta = \frac{g \zeta - \omega(t)/\gamma}{\sqrt{\{g \zeta - \omega(t)/\gamma\}^2 + B_1^2}}. \quad (7)$$

A decay of  $M = |\mathbf{M}|$  during the motion [25] is due to the full spin-lattice relaxation (one component is the spin-lattice relaxation in the rotating frame). An extra defocusing originates from the lack of adiabaticity of the modulation. For our compound, this relaxation rate is slow compare to the modulation frequency. At time  $t = 0$ ,  $B_1$  is assumed to be turned on adiabatically with the sample initially in thermal equilibrium. In this case the norm  $M$  reflects the state of the longitudinal magnetization immediately before the force measurement. During the c.w. sequence, the oscillatory movement of  $M_z(t)$  comes from the  $\cos \theta$  factor. We expand  $\cos \theta \approx a_0 + a_1 \sin(\omega_c t)$  with  $a_1$  the first harmonic Fourier component [26] (higher harmonics have a negligible effect on the motion of the cantilever). Because of the large field inhomogeneities, the amplitude of oscillation depends on the location inside the sample. The resonant sheet, which is the paraboloid of constant  $\zeta_0$ , corresponds to the surface of maximum amplitude of oscillation. The spatial dependence of  $a_1(\zeta)$  is the sensitivity profile. We call  $\Gamma$  the half width at half maximum of this bell-shaped curve.  $\Gamma$  has the units of a distance and it defines the thickness of the slice probed. The amplitude of  $\Gamma$  depends on both  $\Omega$  and  $B_1$ . The induced vibration is synchronously amplified by a lock-in technique. The signal grows exponentially to the asymptotic amplitude

$$A_0 = \frac{1}{\sqrt{2}} \frac{Qg}{k} \int_{V_s} M_0 a_1(\zeta) d\zeta. \quad (8)$$

Thus the peak amplitude of vibration achieved by the cantilever in Fig. 3 is proportional to the longitudinal magnetic moment inside the probed slice at the beginning of the c.w. sequence.

#### 4.3. Spin-spin relaxation measurement

To study the transverse magnetization decay of  $^1\text{H}$  [27] we use a sequence of 3 pulses. A  $\pi/2$  pulse is applied to the spin system, so that the magnetization at  $\zeta_0$  is rotated to the transverse plane. After a fixed delay  $\tau_a$ , a  $\pi$  pulse is applied to form a spin echo. Shortly after, a  $\pi/2$  pulse takes an instant snap-shot of the transverse magnetization by rotating it along  $\mathbf{k}$  and the frozen component is measured with the c.w. sequence described above. Varying the time delay  $\tau_b$  between the last two pulses reconstructs the transient shape of the spin echo.

With increasing spacing  $\tau_a$  between pulses, the size of the spin echo signal decreases due to spin-spin relaxation. Using the same sequence as above, Fig. 5 is a plot of the lock-in peak measured as a function of the time  $2\tau_a$ . We plot the data on a  $x^2\text{-log}(y)$  scale and we find that the decrease follows a Gaussian relaxation  $\exp\{-(t/T_2)^2\}$  with  $T_2 = 39 \pm 1 \mu\text{s}$ . The transverse relaxation  $T_2$  is found to be consistent with conventional NMR detection on a macroscopic sample [28]. With the inferred  $T_2$ , we fit the shape of the echo in Fig. 4 taking into account the dipolar linewidth of the protons in our compound [28] and the spatial dependence  $a_1(\zeta)$ . The solid line in Fig. 4 is the best fit obtained for a sample thickness of  $6.5 \mu\text{m}$  which is in good agreement with the value obtained on the image.

#### 4.4. Spin-lattice relaxation measurement

We now measure the longitudinal magnetization recovery after a saturation comb [29]. The saturation comb is composed of three  $\pi/2$  pulses spaced by  $100 \mu\text{s}$ . The c.w. sequence is applied at a variable delay ( $13 \text{ ms} < t < 20 \text{ s}$ ) after the comb. In order to obtain an intrinsic measurement of the relaxation, it is important to ensure that the sensitivity profile  $a_1(\zeta)$  is exclusively included inside the sample section, otherwise a partial re-polarization of the magnetization occurs during the measurement cycle [27]. For our settings,  $\zeta_0$  is set exactly at the middle of the sample and  $\Gamma = 2.4 \mu\text{m}$  is smaller than the sample thickness. As before, the value plotted is the lock-in output averaged over a 1s time interval around its maximum. We do not detect any signal when  $t = 13 \text{ ms}$ . On Fig. 6, we clearly observe two relaxation times in the recovery process. We fit the results with a double exponential  $\varrho_s\{1 - \exp(-t/T_{1s})\} + (1 - \varrho_s)\{1 - \exp(-t/T_{1l})\}$  which gives  $\varrho_s = 49 \pm 2\%$ ,  $T_{1s} = 0.35 \pm 0.03 \text{ s}$  and  $T_{1l} = 5.4 \pm 0.5 \text{ s}$ . The later value corresponds to the  $T_1$  reported in the literature for this compound [30]. The short relaxation, however, might be due to water contamination inside the crystal during its contact with air. These same two relaxation rates are also measured by conventional NMR in powder samples with particles of dimensions smaller than  $50 \mu\text{m}$  [24].

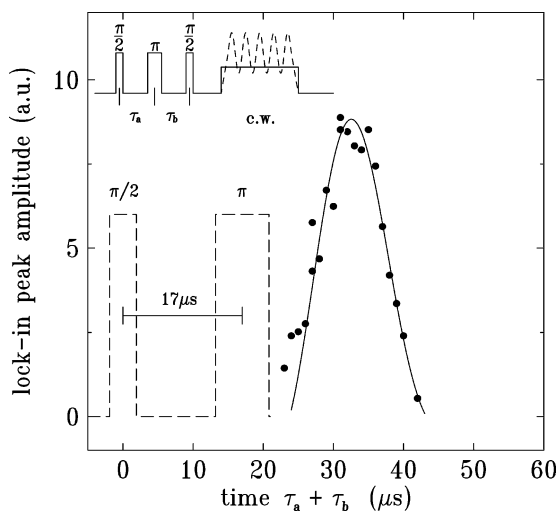


Fig. 4. Measurement of the transient shape of the spin-echo: a  $\pi/2-\tau_a-\pi$  pulse sequence is used to form a spin echo. The transverse magnetization is measured with the combination of a  $\pi/2$  pulse and the c.w. sequence. The amplitude of the force signal is shown as a function of  $\tau_a + \tau_b$  with a fixed  $\tau_a = 17 \mu\text{s}$ . A r.f. field of  $B_1 = 15 \text{ G}$  is used for the pulses. The solid line is a fit of the spin echo shape in our compound for a sample thickness of  $6.5 \mu\text{m}$ .

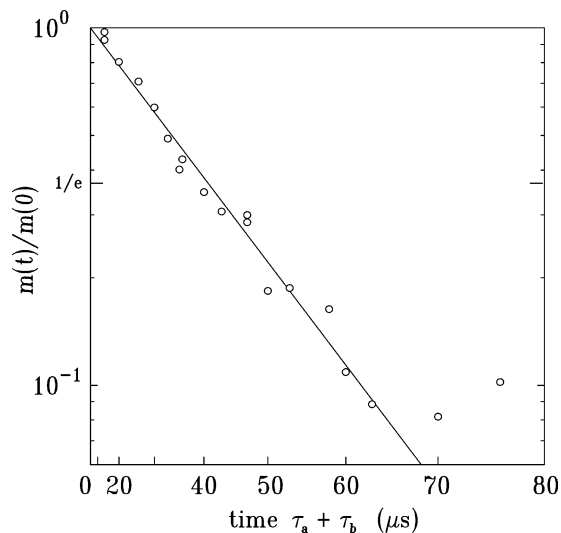


Fig. 5. Spin-spin relaxation time measurement: normalized heights of the spin echo are displayed on a square-logarithmic scale as a function of  $\tau_a + \tau_b$  with  $\tau_a = \tau_b$ . The straight line is a fit with  $\exp\{-(2\tau_a/T_2)^2\}$  where  $T_2 = 39 \pm 1 \mu\text{s}$ .

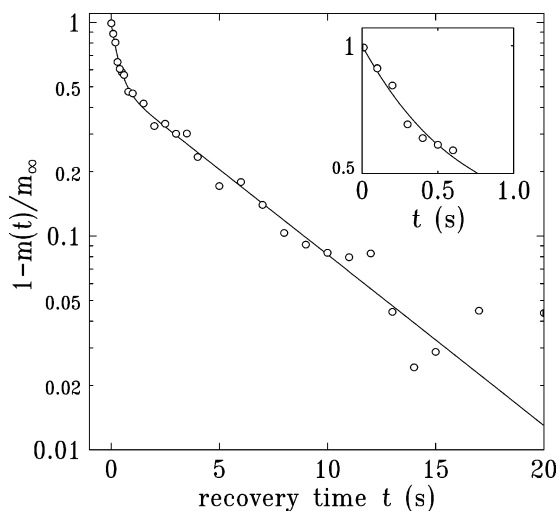


Fig. 6. Measurement of the longitudinal magnetization recovery: the logarithmic of the normalized amplitude of the force signal is shown as a function of the interval between a saturation comb and the c.w. sequence. The solid line is a fit with a double exponential recovery which yields  $T_{1S} = 0.35 \pm 0.03 \text{ s}$  and  $T_{1I} = 5.4 \pm 0.5 \text{ s}$ . Each point is the average of 32 c.w. sequences.

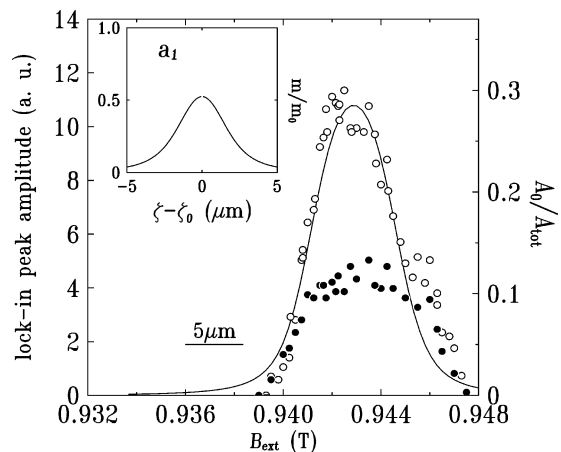


Fig. 7. Force signal as a function of  $B_{\text{ext}}$ : a saturation comb is applied 0.6 s (closed circles) and 16 s (open circles) before the c.w. sequence. The solid line is the expected profile for a parallelepiped sample of  $7 \mu\text{m}$  thickness within both the free spin and adiabatic approximations. The inset shows the spatial dependence of the sensitivity profile of these settings (the transfer function).

#### 4.5. One dimensional imaging of relaxation contrast

One corollary issue concerns the spatial distribution of each spin species inside the sample section. To perform this measurement, we record the amplitude of the lock-in signal as a function of  $B_{\text{ext}}$  for two delays  $t$  between the saturating comb and the c.w. sequence. By sweeping  $B_{\text{ext}}$ , we displace the surface  $\zeta_0$  to a different height in the sample. The force signal

is then proportional to the density of spin around this location. In order to obtain a local measurement, we reduce the thickness  $\Gamma$  of the slice probed by decreasing both  $\Omega$  and  $B_1$  for the c.w. sequence. The inset of Fig. 7 shows the spatial dependence of the sensitivity profile  $a_1(\zeta)$  for our settings where  $\Gamma$ , the half width at half maximum, is  $1.9 \mu\text{m}$ . By using the saturation comb, we can vary the weight  $\rho_s$  of one spin species compared to the other. Qualitatively, the measurement protocol gives more weight to the spin species with short relaxation when the comb is close to the c.w. sequence. We plot in Fig. 7 the obtained results for both  $t = 0.6 \text{ s}$  (closed circles) and  $t = 16 \text{ s}$  (open circles). A rapid glance at the data seems to indicate that the profile of the two sequences are different and we obtain a more rounded profile for the closed circles data suggesting that the water contamination occurs at the surface. The measurements, however, collected close to the edge of the sample are skewed by repolarization processes that modify the shape of the lock-in signal. The solid line is a calculation of the expected profile for a parallelepiped sample of dimensions  $100 \times 50 \times 7 \mu\text{m}^3$  within both the free spin and adiabatic approximations. In spite of the idealized model, the  $t = 16 \text{ s}$  data (open circles) are well described by the calculated profile except for the high field range. The shoulder at large  $B_{\text{ext}}$  corresponds to the surface of the sample that has been glued with epoxy to the cantilever. We did not attempt to fit this part of the data. We assume that the observed step is a signal from the protons in the epoxy.

In conclusion, the experiment above demonstrates that the force detection can achieve the micrometer scale spatial resolution at room temperature and in a 1 T field. Improvements are expected by going to higher field and/or lower temperatures and sub-micron resolutions have been reported with electronic spins [21].

## 5. Spin ordered systems

In the case of ferromagnets, the story is different. Collective modes are excited and the sensitive slice is not simply proportional to the ratio of the linewidth over the field gradient [31]. Furthermore, the longitudinal relaxation time  $T_1$  of ferromagnets cannot be measured by either a standard pulsed decay scheme or a saturation experiment (a measurement of  $h_{\text{sat}}^2 = 1/(\gamma^2 T_1 T_2)$ ), because a premature ‘sticking’ of the transverse magnetization occurs beyond the so-called Suhl threshold [32]. We propose to use a different approach, which is described below.

In a spin ordered state, the spatial fluctuations of the motion (rather than the thermal fluctuations) are the disturbances that may alter the experimentally determined value of the relaxation rate. At the microscopic scale (dimensions smaller than the exchange length), the norm of  $|\mathbf{M}|$  is a constant of the motion and the dissipative term takes the phenomenological Gilbert form [33]. The Gilbert damping coefficient,  $G$ , is the fundamental parameter that characterizes the spin dynamics at this microscopic scale. At the macroscopic scale, we measure the dynamics of a spatially averaged quantity,  $\bar{M}$ . Microscopic relaxation channels are masked by spatial de-coherence of the motion that may lead to an apparent faster decay rate of  $\bar{M}$ . Spatial fluctuations of the motion usually occurs on structural inhomogeneities inside the sample like defects, surface roughness or corners, . . . and these extrinsic effects participate in the broadening of the absorption line.

A direct way of accessing  $G$  is to measure the dynamics of the longitudinal component  $M_z$  [34,35]. In contrast to the transverse magnetization, proportional to the number of magnons in the coherent motion, the diminution of the longitudinal component  $M_s - \bar{M}_z$  is proportional to the total number of magnons excited, including the degenerate magnons that couple to the uniform motion. In other words,  $\bar{M}_z$  approaches equilibrium at the intrinsic spin thermalization rate  $T_1$ , proportional to  $G$  in the small motion limit [36].

In this section, we show how ferromagnetic resonance force microscopy (fMRFM) can be used to measure the intrinsic ferromagnetic relaxation rates inside a micron-size sample. We will present our results obtained at room temperature on a test sample of yttrium iron garnet. The sample is a disk [37] of diameter  $D = 160 \mu\text{m}$  and thickness  $S = 4.75 \mu\text{m}$  perpendicularly magnetized in a static field,  $H_{\text{ext}}$ , of a few kilo Oersted and excited by microwave fields between 5 and 13.5 GHz. Here the permanent magnet [38] is glued at the extremity of the cantilever and then aligned with the axis of the disk. Fig. 1(a) shows a side and top view of the probe magnet attached on the cantilever. It is a cylinder of  $R_{\text{tip}} = 9 \pm 0.5 \mu\text{m}$  in radius and  $L_{\text{tip}} = 32 \pm 3 \mu\text{m}$  in length. The distance between the sample and the probe is fixed at  $\ell = 100 \mu\text{m}$  so that their coupling is in the weak interaction regime [31]. The spatial average of the transverse component of the magnetization,  $\bar{M}_t$ , is measured independently by a standard setup. The power reflected off a half-wavelength resonator is detected by a microwave crystal diode, carefully calibrated so that the signal is square law over the measured range. The diode signal is then proportional to the microwave power absorbed  $P_{\text{abs}} \propto \chi''$ , the imaginary part of the microwave susceptibility. For a magnetization that follows the Bloch’s equation of movement, this quantity varies with  $H_{\text{ext}}$  in the same manner as  $\bar{M}_t^2$ .

In FMR studies, the conventional way of evaluating the damping coefficient is to measure the width of the absorption line at low incident power ( $P_{\text{in}} = 5 \mu\text{W}$  in our case). The shape of the resonance is obtained by scanning the magnetic field  $H_{\text{ext}}$  through the region of resonance when the microwave frequency is maintained constant at the eigen frequency of an almost critically coupled microstrip resonator ( $f_0 = 10.47 \text{ GHz}$ ). For  $\bar{M}_z$ , a substantial gain in sensitivity can be achieved by modulating the magnetization at the fundamental flexure mode of the cantilever,  $\omega_c$ . In this section, we use source modulation, which corresponds to a modulation in amplitude of the incident microwave,  $H_1 \{1 + \varepsilon/2 \cos(\omega_s t) - \varepsilon/2\} \hat{x}$ , with  $\omega_s$  the modulation

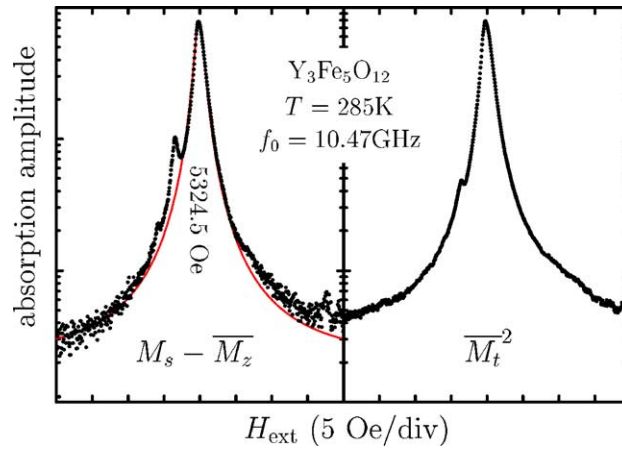


Fig. 8. Line shape of the main resonance absorption line observed simultaneously along the longitudinal and transverse direction at the eigen frequency of the microstrip resonator, 10.47 GHz. The solid line is a fit with a Lorentzian of width 1.57 Oe.

frequency,  $H_1$  the *circularly* polarized amplitude of the microwave field and  $\varepsilon$  the fraction of modulation. This approach is best suited for low power studies (much below the Suhl threshold), as one can take advantage of the full amplitude ( $\varepsilon = 1$ ) without inducing line shape distortion. Fig. 8 displays the measurement of both  $M_s - \bar{M}_z$  ( $M_s$  is the saturation magnetization at the temperature of the experiment) and  $\bar{M}_t^2$  as a function of  $H_{\text{ext}}$  on a semi-logarithmic scale. We observe an intense resonance peak at 5324.5 Oe, the fundamental mode, and all the higher harmonics [37] are outside the figure range. At this power, the shape of the main resonance is identical for both the transverse and longitudinal signal and the main peaks can be fit with the same Lorentzian function of width  $\Delta H = 1.57$  Oe.

For Lorentzian shape, the phenomenological equation of motion of the magnetic moment is the Bloch–Bloembergen form [34]:

$$\frac{d}{dt} \bar{M}_t^2 = 2 \frac{M_s P_{\text{abs}}}{H + 4\pi(n_t - n_z)M_s + H_{\text{anis}}} - 2 \frac{\bar{M}_t^2}{T_2}, \quad (9a)$$

$$\frac{d}{dt} (M_s - \bar{M}_z) = \frac{P_{\text{abs}}}{H + 4\pi(n_t - n_z)M_s + H_{\text{anis}}} - \frac{M_s - \bar{M}_z}{T_1}, \quad (9b)$$

where  $T_2$  and  $T_1$  denote respectively the transverse and longitudinal relaxation times of the magnetization.  $H = H_{\text{ext}} + H_{\text{tip}}$  is the applied magnetic field (not including that of the sample), defined as the superposition of the uniform external field and stray field of the tip along  $z$ ,  $H_{\text{anis}}$  is the magneto-crystalline anisotropy field,  $(n_t, n_z)$  are the depolarization factors respectively transverse and longitudinal, and  $P_{\text{abs}} = \omega_0 \int_{V_s} dV M_y(r) H_1$  expresses the power absorbed inside the sample volume,  $V_s$ . The transverse component of  $\mathbf{H}_{\text{tip}}$  (nul at the center) is neglected. Although this formalism gives a simple relationship between the transverse relaxation rate and the homogeneous line width  $\Delta H_h = 2/(\gamma T_2)$ , it does not include the inhomogeneous broadening nor does it distinguish between the different relaxation channels. Other experiments are then necessary to separate these contributions.

### 5.1. Transverse relaxation measurement

Separation between homogeneous and inhomogeneous broadening can be obtained by performing new experiments in which the amplitude of the longitudinal and transverse component of the magnetization are independently observed for various modulation frequencies around  $1/T_2$  (see Fig. 9(b)). In this fashion, Flechter et al. [35] could extract the relaxation time of all processes other than via the degenerate magnon manifold. Our longitudinal probe uses a narrow band detector limited to the audio frequency range ( $\omega_c/2\pi \approx 3$  kHz). We propose to use a scheme inspired by anharmonic modulation experiments [39]. The h.f. amplitude is fully modulated at an arbitrary frequency  $\omega_s$  while the synthesizer is frequency modulated at  $\omega_f = \omega_s + \omega_c$ . It should be noted that the later approach is equivalent to a modulation of the polarization field.

Fig. 9(c) shows the result for both the transverse and longitudinal signals. The decrease of  $\bar{M}_z$  and  $\bar{M}_t$  with increasing modulation frequency  $\omega_s$  determines the homogeneous part of the broadening  $\Delta H_h$ . Concentrating first on the measurements obtained with a de-tuned circuit (without radiation damping), a fit of 9.8 GHz data gives  $\Delta H_h = 0.7 \pm 0.05$  Oe or  $T_2 = 2/(\gamma \Delta H_h) = 162 \pm 10$  ns. This quantity includes the two-magnon scattering which accounts for 0.2 Oe [40], i.e., a spin-spin relaxation time of  $T_s = 570$  ns. The result is in agreement with Hurben and Patton [41] calculation of the two-magnons

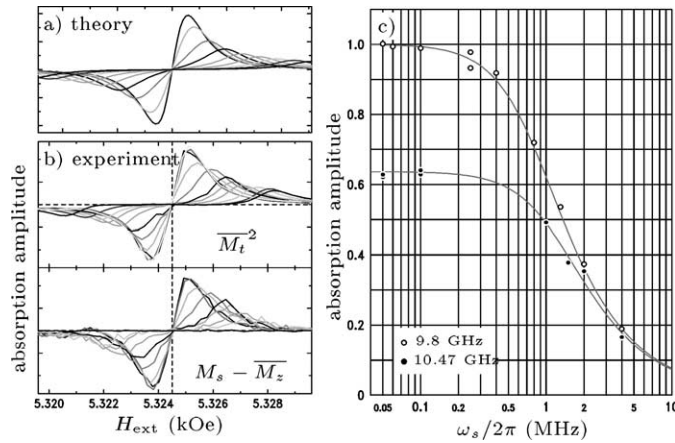


Fig. 9. (a) Theoretical and (b) experimental distortion of the anharmonic absorption line (longitudinal and transverse) for different modulation frequencies between 0.1 and 10 MHz in steps of 1 MHz. The amplitude of the frequency modulation corresponds to 10% of the line width. (c) Diminution of the absorption amplitude with increasing modulation frequency. The width of the 9.8 GHz bell curve gives the transverse relaxation time,  $T_2 = 162$  ns. The 10.47 GHz data are normalized to the width to illustrate the effects of radiation damping.

contribution for a normally magnetized disk of finite aspect ratio. The contribution is small because the resonance frequency of the main mode lies at the lowest point of the spin wave spectrum so that the degenerate magnon manifold has shrunk to almost a point [42].

## 5.2. Spin-lattice relaxation measurement

To assess  $T_1$  directly, we propose to use our quantitative measurements of  $\overline{M}_z$  [43], the spatial average of the longitudinal magnetization. At resonance,

$$T_1 P_{\text{abs}} = \int_{V_s} dV \{M_s - M_z(r)\} \{H(r) - 4\pi n_z(r) M_s\}, \quad (10)$$

which can be interpreted by saying that the energy that is transferred to the lattice in the time  $T_1$  is equal to the diminution of magnetic energy stored in the sample. The important point is that it affords a direct method of measuring the spin-lattice relaxation rate at a fixed frequency. For small precession angle,  $\theta \ll 1$ , the above formula can be more readily rewritten in the form  $T_1 \approx (M_s - \overline{M}_z)/(\gamma^2 H_1^2 T_2 M_s)$ . We find  $T_1 = 95 \pm 10$  ns [43]. The value is approximately equal to  $T_2/2$  which confirms that, for our geometry, the energy flows directly into lattice motions and the decay into non-uniform magnetic modes is small. Taking into account the frequency dependence of  $T_1$ , the obtained result compares well with the  $T_1 = 137$  ns measured by Flechter et al. [35] at 6.2 GHz, but part of this agreement is somewhat coincidental since it depends on the sample quality.

## 6. Conclusion

From both an analytical and experimental point of view, magnetic resonance force microscope is a measurement method that provides a substantial improvement in sensitivity compare to a conventional inductive technique. As shown in this article, the fact that it measures the longitudinal component of the magnetization does not prevent a complete characterization of the relaxation times inside the spin systems. Moreover, in the case of ferromagnet, it gives a direct access to spin-lattice relaxation, a quantity which is proportional to the intrinsic Gilbert coefficient.

## Acknowledgements

The authors are grateful to C. Fermon, M. Goldman, V. Charbois, G. de Loubens, O. Acher, J. Ben Youssef, and H. Le Gall for their help in this research. This work was partially supported by the E.U. project M<sup>2</sup>EMS (IST-2001-34594) and the Action Concertée Nanoscience NN085.

## References

- [1] P.C. Lauterbur, *Nature* 242 (1973) 190.
- [2] P. Mansfield, P.K. Granel, *J. Phys. C* 6 (1973) L422.
- [3] D.F. Evans, *Phil. Mag.* 1 (1956) 370.
- [4] G. Alzetta, E. Arimondo, C. Ascoli, A. Gozzini, *Nuovo Cimento* 52B (1967) 392.
- [5] G. Alzetta, E. Arimondo, C. Ascoli, *Nuovo Cimento* 54B (1968) 107.
- [6] J.A. Sidles, *Appl. Phys. Lett.* 58 (1991) 2854.
- [7] J.A. Sidles, D. Rugar, *Phys. Rev. Lett.* 70 (1993) 3506.
- [8] J.A. Sidles, J.L. Garbini, K.J. Bruland, D. Rugar, O. Züger, S. Hoen, C.S. Yannoni, *Rev. Mod. Phys.* 67 (1995) 249.
- [9] D. Rugar, C.S. Yannoni, J.A. Sidles, *Nature* 360 (1992) 563.
- [10] D. Rugar, O. Züger, S. Hoen, C.S. Yannoni, H.M. Vieth, R.D. Kendrick, *Science* 264 (1994) 1560.
- [11] P. Poncharal, Z.L. Wang, D. Ugarte, W.A. de Heer, *Science* 283 (1999) 1513.
- [12] B. Reulet, A.Y. Kasumov, M. Kociak, R. Deblock, I.I. Khodos, Y.B. Gorbatov, V.T. Volkov, C. Journet, H. Bouchiat, *Phys. Rev. Lett.* 85 (2000) 2829.
- [13] D.L. Olson, T.L. Peck, A.G. Webb, R.L. Magin, J.V. Sweedler, *Science* 270 (1995) 1967.
- [14] J.E. Stocker, T.L. Peck, A.G. Webb, R.L. Magin, *IEEE Trans. Biomedical Eng.* 44 (1997) 1122.
- [15] K.Y. Yasumura, T.D. Stowe, E.M. Chow, T. Pfafman, T.W. Kenny, B.C. Stipe, D. Rugar, *IEEE JMEMS* 9 (2000) 117.
- [16] T.L. Peck, R.L. Magin, J. Kruse, M. Feng, *IEEE Trans. Biomed. Eng.* 41 (1994) 706.
- [17] R.D. Black, T.A. Early, P.B. Roemer, O.M. Mueller, A. Mogro-Campero, L.G. Turner, G.A. Johnson, *Science* 259 (1993) 793.
- [18] W.-C. Lin, G. K. Fedder, *Tech. Rep. CMU-RI-TR-01-06*, Robotics Institute, Carnegie Mellon University, Pittsburgh, PA, March 2001.
- [19] C. Poole, *Electron Spin Resonance*, Interscience, New York, 1975, p. 296.
- [20] D. Mozysky, I. Martin, P.C. Pelekhov, D. Hammel, *Appl. Phys. Lett.* 82 (2003) 1278.
- [21] B.C. Stipe, H.J. Mamin, T.D. Stowe, T.W. Kenny, D. Rugar, *Phys. Rev. Lett.* 86 (2001) 2874.
- [22] H.J. Marmin, R. Budakian, B.W. Chui, D. Rugar, *Phys. Rev. Lett.* 91 (2003) 207604.
- [23] J.G. Kempf, J.A. Marohn, *Phys. Rev. Lett.* 90 (2003) 087601.
- [24] O. Klein, V.V. Naletov, H. Alloul, *Eur. Phys. J. B* 17 (2000) 57.
- [25] A. Abragam, *Principles of Nuclear Magnetism*, Oxford University Press, 1961.
- [26] O. Züger, S.T. Hoen, C.S. Yannoni, D. Rugar, *J. Appl. Phys.* 79 (1996) 1881.
- [27] K. Wago, D. Botkin, C.S. Yannoni, D. Rugar, *Phys. Rev. B* 57 (1998) 1108.
- [28] R.E. Richards, T. Scafer, *Trans. Faraday Soc.* 57 (1961) 210.
- [29] E. Fukushima, S.B.W. Roeder, *Experimental Pulse NMR*, Addison-Wesley, 1981.
- [30] D.E. O'Reilly, T. Tsang, *J. Chem. Phys.* 46 (1967) 1291.
- [31] Z. Zhang, P.C. Hammel, P.E. Wigen, *Appl. Phys. Lett.* 68 (1996) 2005;  
V. Charbois, V.V. Naletov, J. Ben Youssef, O. Klein, *Appl. Phys. Lett.* 80 (2002) 4795.
- [32] H. Suhl, *J. Phys. Chem. Solids* 1 (1957) 209.
- [33] T.L. Gilbert, *Phys. Rev.* 100 (1955) 1243.
- [34] N. Bloembergen, S. Wang, *Phys. Rev.* 93 (1954) 72.
- [35] R.C. Flechter, R.C. LeCraw, E.G. Spencer, *Phys. Rev.* 117 (1960) 955.
- [36] W.K. Hiebert, A. Stankiewicz, M.R. Freeman, *Phys. Rev. Lett.* 79 (1997) 1134.
- [37] V. Charbois, V.V. Naletov, J. Ben Youssef, O. Klein, *J. Appl. Phys.* 91 (2002) 7337.
- [38] M.J. Malliavin, O. Acher, C. Boscher, F. Bertin, V. Larin, *J. Magn. Magn. Mater.* 196 (1999) 420.
- [39] K.J. Bruland, J. Krzystek, J.L. Garbini, J.A. Sidles, *Rev. Sci. Instrum.* 66 (1995) 2853.
- [40] O. Klein, V. Charbois, V.V. Naletov, C. Fermon, *Phys. Rev. B (Rapid Comm.)* 67 (2003) 220407.
- [41] M.J. Hurben, C.E. Patton, *J. Appl. Phys.* 83 (1998) 4344.
- [42] M. Sparks, *Ferromagnetic Relaxation Theory*, McGraw-Hill, 1964.
- [43] V.V. Naletov, V. Charbois, O. Klein, C. Fermon, *Appl. Phys. Lett.* 83 (2003) 3132.